Contents lists available at ScienceDirect

Materials Science in Semiconductor Processing

journal homepage: www.elsevier.com/locate/mssp

Full length article

Raman activity, piezoelectric response, and carrier mobility in two-dimensional Janus TiGeZ_3H (Z = N, P, As) semiconductors: A first-principles prediction

A.I. Kartamyshev [a,b], Nguyen N. Hieu [c,d,*], N.A. Poklonski [e], Nguyen V. Hieu [f], Tuan V. Vu [a,b], A.A. Lavrentyev [g], Huynh V. Phuc [h,**]

[a] Laboratory for Computational Physics, Institute for Computational Science and Artificial Intelligence, Van Lang University, Ho Chi Minh City, Viet Nam
[b] Faculty of Mechanical - Electrical and Computer Engineering, School of Technology, Van Lang University, Ho Chi Minh City, Viet Nam
[c] Institute of Research and Development, Duy Tan University, Da Nang, Viet Nam
[d] Faculty of Natural Sciences, Duy Tan University, Da Nang, Viet Nam
[e] Faculty of Physics, Belarusian State University, Minsk 220030, Belarus
[f] The University of Danang - University of Science and Education, Da Nang, Viet Nam
[g] Department of Electrical Engineering & Electronics, Don State Technical University, 344010 Rostov-on-Don, Russian Federation
[h] Division of Physics, School of Education, Dong Thap University, Cao Lanh, Viet Nam

ARTICLE INFO

Keywords:
Two-dimensional Janus materials
Raman activity
Piezoelectricity
Electronic states
Carrier mobility

ABSTRACT

In this article, we theoretically propose a series of TiGeZ_3H (Z = N, P, As) monolayers and comprehensively investigate their structural, vibrational, piezoelectric, electronic, and transport properties using first-principles simulations. The structural stability of the suggested monolayers is verified by phonon dispersion analysis, *ab-initio* molecular dynamics calculations, and Born–Huang mechanical stability criteria. Based on the calculations for the mechanical response, it is shown that TiGeN_3H is the stiffest material compared to the other two structures with Young's modulus found to be 252.11 Nm^{-1}. Besides, we also examine the vibrational characteristics of TiGeZ_3H through the analysis of their phonon spectra and Raman active modes. Due to the broken vertical mirror symmetry, TiGeZ_3H monolayers possess both out-of-plane and in-plane piezoelectric responses, in particular, the out-of-plane piezoelectric coefficient of TiGeAs_3H is computed to be up to −0.42 pm/V. Janus TiGeZ_3H monolayers are found to be indirect semiconductors with decreasing bandgap as Z changes from N to As. Particularly, the Rashba spin splitting is found in TiGeAs_3H when the spin–orbit coupling is taken into account. The calculations for the transport features indicate that while TiGeN_3H monolayer exhibits low electron mobility, both TiGeP_3H and TiGeAs_3H have electron mobility μ_x over 400 cm^{2}V^{-1}s^{-1}, which is suitable for applications in electronics.

1. Introduction

The successful fabrication of graphene monolayer is an important milestone in the fields of material sciences, especially layered two-dimensional (2D) nanostructures [1]. Over time, 2D layered materials have shown that they are versatile materials with diverse crystal structures [2–4]. The physical properties of 2D materials depend significantly on the composition of the compound, the number of atomic layers, the symmetry of the structure, and so on [5,6]. Recently, a high-quality $MoSi_2N_4$ monolayer was successfully synthesized by the common experimental method, namely chemical vapor deposition [7], creating a new 2D material family called the MA_2Z_4 family (M belongs to transition metals, A is C, Si, or Ge, and Z refers to a pnictogen atom N, P, or As) [8]. MA_2Z_4 materials have attracted the community's attention because they have many extraordinary physical characteristics. For example, a septuple-atomic-layer $MoSi_2N_4$ monolayer, which can be formed by stacking MoN_2 layer between two Si–N bilayers, is a nonmagnetic semiconductor [7,8] even though MoN_2 is a ferromagnetic metal [9]. MA_2Z_4 monolayers exhibit a good Raman intensity [10] and high lattice thermal conductivity [11].

Due to the diversities of composition in the compound, MA_2Z_4 materials are a significant category of 2D materials that provide specifically customized physical characteristics to fulfill the requirements of various applications. Furthermore, the MA_2Z_4-based heterostructures

* Corresponding author at: Institute of Research and Development, Duy Tan University, Da Nang, Viet Nam.
** Corresponding author.
E-mail addresses: andrey.kartamyshev@vlu.edu.vn (A.I. Kartamyshev), hieunn@duytan.edu.vn (N.N. Hieu), hvphuc@dthu.edu.vn (H.V. Phuc).

https://doi.org/10.1016/j.mssp.2024.109102
Received 9 October 2024; Received in revised form 29 October 2024; Accepted 6 November 2024

have many outstanding features, such as $MoSi_2N_4/NbS_2$ possesses an ultra-low Schottky barrier height [12], $MoSi_2N_4/MoS_2$ heterostructure possesses large photocurrent density up to 1.6 mA cm^{-2} [13], or $MoGe_2N_4$/BP heterostructure is predicted to be suitable for optoelectronic device applications [14]. More specifically, several asymmetric Janus structures based on MA_2Z_4, such as $XMoSiN_2$ (X = S, Se, Te) [15], $WSiGeN_4$ [16], or $HfSiGeN_4$ [17], have been modeled and theoretical calculations have shown that these structures have a stable crystalline structure with superior physical features. Motivated by the successful experimental synthesis of Janus asymmetric structures, namely Janus MoSSe [18,19], theoretical and modeling studies on 2D asymmetric structures, including Janus based-MA_2Z_4 materials [20, 21], have received increasing attention. Recent research results show great application prospects of asymmetric structures in various fields of electronics, spintronics, and optoelectronics [22,23].

Here, we theoretically propose a series of $TiGeZ_3H$ (Z = N, P, As) monolayers and comprehensively explore their structural stability, vibrational characteristics and Raman activities, piezoelectricity, electronic properties, and carrier mobility via first-principles simulations. Our computed results reveal that $TiGeZ_3H$ monolayer, which can be made from $TiGe_2Z_4$ monolayer by substituting the top S–N layer with one H layer, has a stable crystal structure and good Raman activities. Janus $TiGeZ_3H$ monolayers shows a remarkably piezoelectric response and high electron mobility.

2. Computational details

All first-principles simulations were conducted using density functional theory (DFT) with the projector augmented wave (PAW) technique [24,25], as implemented in the Vienna *ab initio* simulation package (VASP) [26,27]. The exchange–correlation energy was evaluated using the generalized gradient approximation (GGA) proposed by Perdew, Burke, and Ernzerhof (PBE) [28]. To enhance the comprehensive examination of the electronic bandgap, we incorporated the hybrid functional suggested by Heyd, Scuseria, and Ernzerhof (HSE06) [29]. The self-consistent calculations incorporated the inclusion of the spin–orbit coupling (SOC) [30]. A cutoff energy of 600 eV was chosen for the plane-wave basis set and the integration of the Brillouin zone (BZ) was performed using a 12 × 12 × 1 k-point mesh grid. A convergence threshold of 10^{-6} eV was chosen for the total energy and the positions of the atoms were loosened until the Hellmann–Feynman forces on each atom were smaller than 10^{-3} eV/Å during the structural optimization. To prevent interactions between periodic slabs, a vacuum space of 30 Å was introduced vertically. We used the finite displacement technique to examine the phonon dispersion based on PHONOPY code [31]. A 4 × 4 × 1 supercell was employed for calculations of the phonon spectrum. The *ab initio* molecular dynamics (AIMD) simulation was examined at a constant temperature of 300 K with a canonical ensemble to test the thermal stability of the investigated structures. The total test time is 10 ps with a time step of 1 fs. We used the dipole layer method, which was implemented in the VASP, to correct the dipole moment resulting from the broken mirror symmetry in Janus structures. The finite displacement technique implemented in the VASP was used to calculate the Raman activities in the proposed structures. The Raman activity of each phonon branch at the Γ point in the BZ was obtained by taking the derivative of the macroscopic dielectric tensor [32]. The elastic and piezoelectric coefficients were evaluated by employing strain–stress relationships and density functional perturbation theory (DFPT). In order to examine the carrier mobilities, we used the deformation potential (DP) method as described by Bardeen and Schokley [33].

3. Results and discussion

3.1. Crystal structure and stability

Crystal structures of $TiGeZ_3H$ (Z = N, P, and As) monolayers are depicted in Fig. 1. The unit-cell of $TiGeZ_3H$ contains six atoms, including one Ti, one Ge, one H, and three Z atoms. The crystal structure of $TiGeZ_3H$ monolayer belongs to the $P3m1$ space symmetry group. The lattice constants a of $TiGeZ_3H$ monolayers are simulated to be 3.03, 3.62, and 3.76 Å corresponding to Z = N, P, and As, respectively. The value of a for $TiGeZ_3H$ increases with the increase in the size of the atomic radius of Z atom from N to As. Table 1 reveals the computed results for the crystal structure parameters for $TiGeZ_3H$ monolayers. It is demonstrated that the monolayer thickness Δh of $TiGeN_3H$, $TiGeP_3H$, and $TiGeAs_3H$ monolayers are 5.81, 7.53, and 7.97 Å, respectively. The large differences in thickness between studied monolayers are due to large differences correspondingly in the interatomic bond lengths between the monolayers. For example, the Z–H bond length d_1 for $TiGeN_3H$ is 1.03 Å, which is much smaller than that for $TiGeAs_3H$ (1.53 Å), as revealed in Table 1. It should also be noted that the Janus $ZrGeZ_3H$ (Z = N, P, and As) structures have also been reported in a recent work [34]. However, with the large difference in atomic size between Ti and Zr, there should be a large difference in the lattice constants of $TiGeZ_3H$ and $ZrGeZ_3H$. For example, the lattice constant of $TiGeN_3H$ is 3.03 Å, which is significant smaller than that of ZrGeN3H (3.18 Å) [34]. Since the physical properties, especially the electronic and transport properties of 2D materials are highly dependent on the perfection of the crystal structure, the difference in crystal structure between these two groups of materials can lead to many differences in their physical properties.

To evaluate the physical viability of $TiGeZ_3H$ monolayers, we systematically test the stability of their crystalline structure. Firstly, we analyze the cohesive energy per atom E_{coh} to evaluate the strength of the interatomic chemical bonding in the studied structures. For $TiGeZ_3H$ monolayers, E_{coh} can be calculated via the expression as:

$$E_{coh} = \frac{(N_{Ti}E_{Ti} + N_{Ge}E_{Ge} + N_Z E_Z + N_H E_H) - E_{tot}}{N_{Ti} + N_{Ge} + N_Z + N_H}, \quad (1)$$

where E_{tot} is the monolayer total energy. The energy of the isolated element $\mathcal{A}$ ($\mathcal{A}$ = Ti, Ge, Z, and H) is denoted by $E_{\mathcal{A}}$ and $N_{\mathcal{A}}$ indicates the number of $\mathcal{A}$ atoms in the unitcell.

The computed values of E_{coh} for $TiGeZ_3H$ are revealed in Table 1. It is indicated that the values of E_{coh} for $TiGeN_3H$, $TiGeP_3H$, and $TiGeAs_3H$ monolayers are 6.85, 5.12, and 4.68 eV/atom, respectively. The positive value of E_{coh} confirms the energetic stability of $TiGeZ_3H$. The value of E_{coh} for Janus $TiGeN_3H$ is estimated to be 6.85 eV/atom, which is higher than that of $TiGeP_3H$, and $TiGeAs_3H$ monolayers, implying that $TiGeN_3H$ is more energetically stable than $TiGeP_3H$ and $TiGeAs_3H$ monolayers. The greater the cohesion energy, the stronger the chemical bond. Computed results show that the chemical bonds in $TiGeN_3H$ are the strongest, which is consistent with the obtained results for structural parameters that the length of the chemical bonds in $TiGeN_3H$ monolayer are shorter than those in other studied materials.

To provide further context for understanding the nature of the chemical bonding, we show the electron localization function (ELF) of $TiGeZ_3H$ in Fig. 1(b). In the ELF contours, the electron accumulation/depletion is denoted by the blue/red color. It is demonstrated that strong electron localization is found near the hydrogen atom. Also, we can see a high charge density around the Z atoms, specifically the $Z(3)$ atom (bottom Z atom). Meanwhile, a quite low charge density is found around both Si and Ge atoms.

In Fig. 1(c), we reveal the phonon dispersion of $TiGeZ_3H$ to analyze their dynamical stabilities. Due to the unitcell containing six atoms, phonon dispersion of $TiGeZ_3H$ has 18 vibrational modes. Three acoustic phonon modes are found in the low-frequency region. There are 15 optical phonon modes are available in the higher regions. It is demonstrated that there is no phononic gap between acoustic optical phonon vibrations, suggesting the strong optical-acoustic scattering available in $TiGeZ_3H$ monolayers. With strong optical-acoustic scattering, $TiGeZ_3H$ monolayers can be exhibited low-thermal conductivity. However, one distinct phononic gap in the optical vibrational region is observed in all three studied structures. This distinct phononic gap is found within the frequency ranges of 850–3350, 500–2300, and 400–2100 cm^{-1}

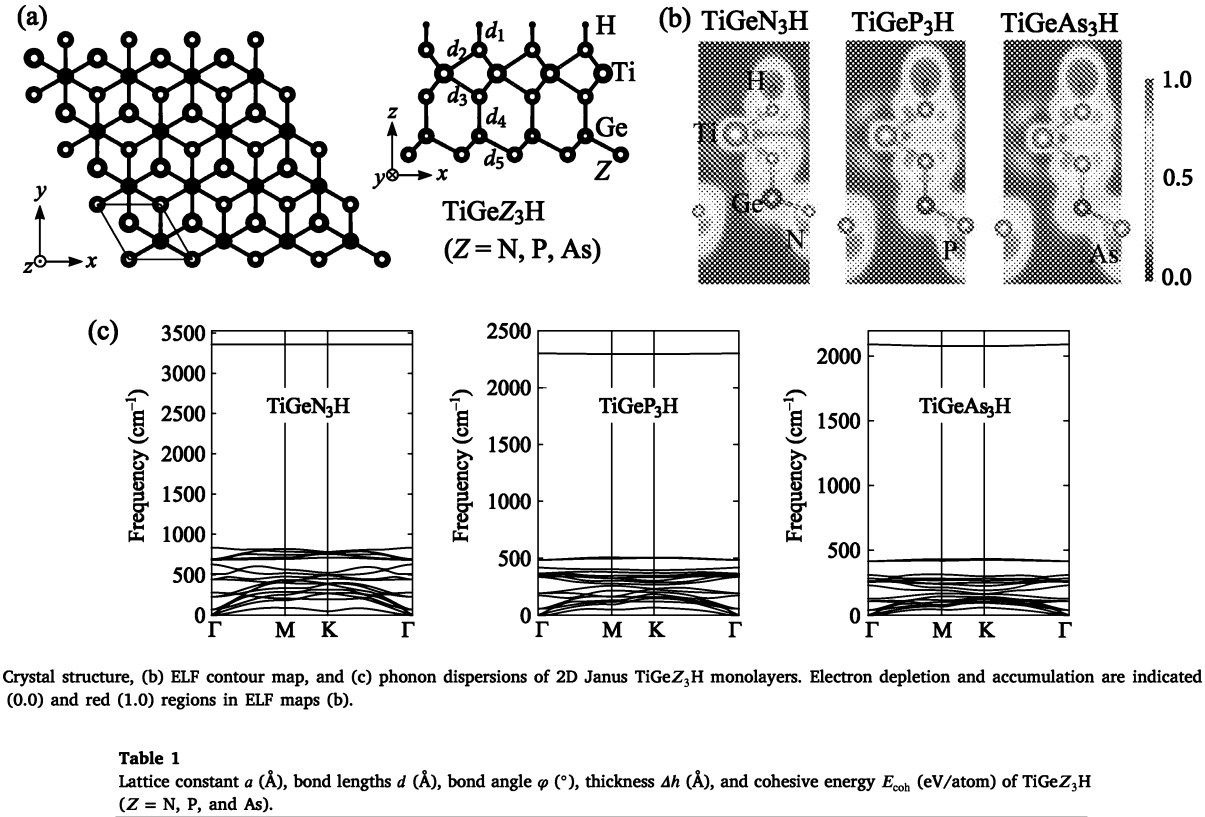

Fig. 1. (a) Crystal structure, (b) ELF contour map, and (c) phonon dispersions of 2D Janus TiGeZ_3H monolayers. Electron depletion and accumulation are indicated respectively by the blue (0.0) and red (1.0) regions in ELF maps (b).

Table 1
Lattice constant a (Å), bond lengths d (Å), bond angle φ (°), thickness Δh (Å), and cohesive energy E_{coh} (eV/atom) of TiGeZ_3H (Z = N, P, and As).

	a	d_1	d_2	d_3	d_4	d_5	$\varphi_{\angle H-Z-Ti}$	$\varphi_{\angle Z-Ti-Z}$	$\varphi_{\angle Ti-Z-Ge}$	$\varphi_{\angle Z-Ge-Z}$	Δh	E_{coh}
$TiGeN_3H$	3.03	1.03	2.09	2.10	1.88	1.86	122.90	66.23	123.33	109.62	5.81	6.85
$TiGeP_3H$	3.62	1.42	2.51	2.49	2.31	2.34	123.49	66.34	122.84	116.88	7.53	5.12
$TiGeAs_3H$	3.76	1.53	2.61	2.59	2.42	2.45	123.81	66.91	123.10	117.80	7.97	4.68

for $TiGeN_3H$, $TiGeP_3H$, and $TiGeAs_3H$, respectively. The presence of this large gap is a consequence of the differences in the atomic mass between the constituent elements in the considered structures.

It is important to note that no soft modes (imaginary frequency) are available in the phonon spectra of studied TiGeZ_3H materials. The negative frequencies are the signal that the studied structure might be unstable because the restore forces, which are against the atom displacement, are eliminated. Obtained results for phonon dispersion indicate that TiGeZ_3H monolayers are all dynamically stable. Besides, the AIMD test is performed to analysis of the thermal stabilities of TiGeZ_3H materials. In Fig. 2, we present the obtained simulations for the total energy variations to time at room temperature of TiGeZ_3H monolayers by the AIMD. It is revealed that the total energies of TiGeZ_3H monolayers change slightly, only about 0.5 eV, within 10 ps period of the AIMD test. The crystalline structures after 10 ps of the TiGeZ_3H monolayers remained robust. Neither the breaking of chemical bonds nor any structural phase transition was detected. This confirms the thermodynamical stability of the studied materials at room temperature.

3.2. Raman active modes and vibrational properties

When figuring out the physical characteristics of materials, the Raman spectrum is extremely important. Raman spectroscopy is a non-destructive analytical technique that provides detailed information about the structural and physical properties of the considered materials [35]. One can use Raman spectroscopy to distinguish between different crystalline phases of a material [36,37]. The number of layers in 2D layered structures can be determined by Raman spectroscopy [38, 39]. The intensity and position of certain Raman peaks are sensitive to the layer thickness [40]. Besides measuring the Raman spectrum experimentally, we can determine the Raman activities of materials by DFT calculations through deriving the macroscopic dielectric tensor at the Γ point within small difference method [41]. Since the symmetry of TiGeZ_3H (Z = N, P, As) monolayers belong to $P3m1$ (No. 156) space group, the corresponding irreducible representation of the phonon branches at the Γ point can be represented as $\Gamma_{phonon} = 6A_1 + 6E$. Here, A_1 vibrational modes are assigned to non-degenerate vibrations along the vertical direction and E modes refer to doubly degenerate in-plane vibrations. The acoustic vibrations contain one A_1 phonon mode and one E phonon mode. The irreducible representation for optical modes can be shown as:

$$\Gamma_{optic} = 5A_1 + 5E. \quad (2)$$

In the materials with $P3m1$ space group, both A_1 and E modes are found as Raman actives, implying that we can detect them by Raman spectroscopy. Fig. 3 represents the Γ-centered Raman spectra and the corresponding atomic displacements of the optical vibrations in Janus TiGeZ_3H monolayers. The Raman spectrum of TiGeZ_3H principally contains ten peaks. Our calculations indicate that while some Raman peaks in $TiGeP_3H$ and $TiGeAs_3H$ monolayers are weak in intensity, all 10 peaks in the Raman spectrum of $TiGeN_3H$ monolayer can be clearly observed as depicted in Fig. 3(a). In the Raman spectrum of $TiGeN_3H$, the fourth A_1 vibrational mode (at a frequency of 832 cm^{-1}) is very robust. Meanwhile, the most robust mode in the Raman spectrum for $TiGeP_3H$ and $TiGeAs_3H$ is the second A_1 modes at frequencies of 351 and 230 cm^{-1}, respectively. These A_1 modes are mainly attributed to the out-of-plane vibrations of Z atoms. In the case of $TiGeAs_3H$, the third A_1 mode, which is significantly attributed to the out-of-plane vibrations of the Ti atom, is also highly robust. In all three studied structures, the intensity of E modes, which arise from in-plane vibrations of the atoms, is generally weaker than that of A_1 modes. From

Table 2
The relaxed-ion elastic stiffness coefficient C_{ij}, Young's modulus Y_{2D}, Poisson ratio ν, and piezoelectric coefficients e_{11}, e_{31}, d_{11}, and d_{31} of 2D Janus TiGeZ_3H materials.

	C_{11} (N/m)	C_{12} (N/m)	C_{66} (N/m)	Y_{2D} (N/m)	ν	e_{11} 10^{-10} C/m	e_{31} 10^{-10} C/m	d_{11} (pm/V)	d_{31} (pm/V)
$TiGeN_3H$	286.87	99.57	93.56	252.11	0.35	2.80	−0.22	1.50	−0.07
$TiGeP_3H$	116.18	36.94	39.62	104.44	0.32	−0.65	−0.44	−0.82	−0.29
$TiGeAs_3H$	100.03	35.83	32.10	87.20	0.36	−1.05	−0.58	−0.58	−0.42

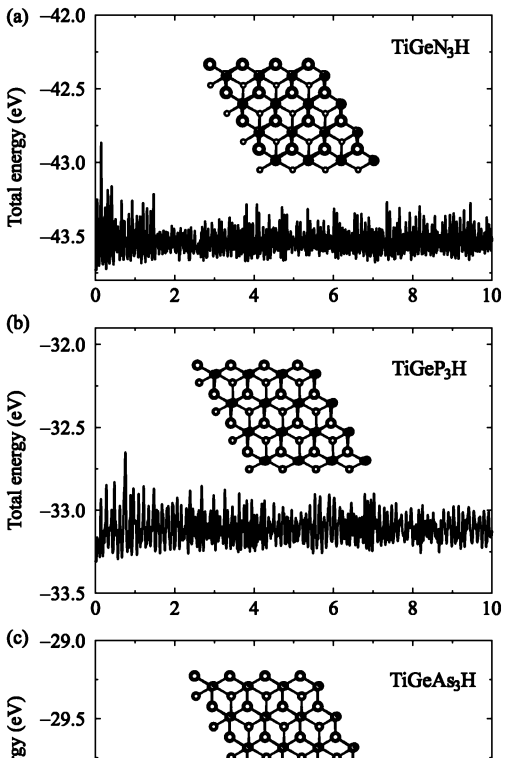

Fig. 2. The time-dependence of the total energies of TiSiZ_3H monolayers at room temperature by AIMD tests. Insets indicate the crystal structure of TiSiZ_3H at 10 ps.

Fig. 3, we can see that the A_1 phonon mode is the highest optical mode for all three Janus structures. There is a strong association between the redshift observed in the Raman spectra of TiGeZ_3H monolayers and the increase in the atomic size of the Z atoms from N to As. The highest optical mode A_1 (the fifth A_1 mode) is observed at frequencies of 3372, 2311, and 2100 cm^{-1}, respectively.

3.3. Mechanical characteristics and piezoelectric response

In this part, we examine the mechanical characteristics of TiGeZ_3H monolayers. The elastic coefficients C_{ij} (using Voigt's notation) are determined by analyzing the uniaxial strain-dependent unit-cell energy [42]. The computed results for the elastic coefficients C_{ij} of TiGeZ_3H materials are presented in Table 2. It is shown that $TiGeN_3H$ possesses high elastic coefficients with C_{11} = 286.87 N/m and C_{12} = 93.56 N/m. Meanwhile, the calculated values for $C_{11}(C_{12})$ of $TiGeP_3H$ and $TiGeAs_3H$ monolayers are found to be 116.18(36.94) and 100.03(35.83) N/m, respectively. The obtained results for C_{ij} satisfy the Born-Huang criteria of the 2D hexagonal structures $[(C_{11}^2 - C_{12}^2) > 0$ and $C_{66} > 0]$ [43,44], suggesting the mechanical stability of TiGeZ_3H monolayers.

From obtained elastic stiffness coefficients C_{ij}, we can analyze the fundamental features of TiGeZ_3H, including Young's modulus Y_{2D} and Poisson's ratio ν, which are written as

$$Y_{2D} = \frac{C_{11}^2 - C_{12}^2}{C_{11}}, \tag{3}$$

$$\nu = \frac{C_{12}}{C_{11}}. \tag{4}$$

As indicated in Table 2, $TiGeN_3H$ has a high Young's modulus, up to 252.11 N/m. It is known that the higher Y_{2D} indicates stronger resistance of material against the applied forces. Meanwhile, both $TiGeP_3H$ and $TiGeAs_3H$ monolayers are mechanically softer than $TiGeN_3H$ with Y_{2D} of 104.44 and 87.20 N/m, respectively, as revealed in Table 2. The computed values of ν for $TiGeN_3H$, $TiGeP_3H$, and $TiGeAs_3H$ are found to be 0.35, 0.32, and 0.36, respectively. Obviously, TiGeZ_3H monolayers possess a high Poisson ratio, demonstrating the ductile character of the studied structures. With a large Poisson's ratio, TiGeZ_3H monolayers easily respond to induced uniaxial strains.

The piezoelectric effect plays a decisive role in the use of material in applications that convert mechanical to electrical energy and vice versa. The piezoelectric effect is a unique characteristic of some materials where an electric dipole moment is created when external stress is applied, and vice versa. This phenomenon occurs specifically in noncentrosymmetric materials. Recent studies, both experimental and theoretical, show that two-dimensional materials have a more prominent piezoelectric effect than their corresponding bulk forms [45–48]. As shown in Fig. 1(a), Janus TiGeZ_3H has a non-centrosymmetric structure and we can treat TiGeZ_3H as piezoelectric materials with both in-plane and out-of-plane piezoelectricity. As a ground state property, the piezoelectricity can be calculated using the DFT method. Importantly, the recently experimentally measured piezoelectric coefficients of MoS_2 [49] are in good consistent with previous DFT prediction released by Duerloo et al. [42]. In this study, we use the computational techniques proposed by Duerloo et al. [42] to examine the piezoelectricity of Janus TiGeZ_3H monolayers.

In non-centrosymmetric materials, applying uniaxial strains can alter the polarization. According to the modern theories of polarization [50], linear piezoelectricity can be determined by the uniaxial strain-dependence of polarization. The linear piezoelectricity can be analyzed via the third-rank piezoelectric stress e_{ijk} and strain d_{ijk} tensors. We can calculate these piezoelectric tensors based on the relationship with the surface electrical polarization P_i and strain/stress $\varepsilon_{jk}/\sigma_{jk}$ tensor as [42]:

$$e_{ijk} = \frac{\partial P_i}{\partial \varepsilon_{jk}}, \tag{5}$$

$$d_{ijk} = \frac{\partial P_i}{\partial \sigma_{jk}}, \tag{6}$$

where $i, j, k \in \{1, 2, 3\}$ with 1, 2, and 3 referring respectively to Cartesian directions x, y, and z. The piezoelectric stress tensor in 2D structures e_{ij} needs to be renormalized by the unit of lattice parameter along the z direction, namely $e_{ij}^{2D} = z \cdot e_{ij}^{3D}$. We calculate the e_{ij} through density functional perturbation theory (DFPT) method. It is worth mentioning that the orthorhombic supercell is utilized for calculating the piezoelectric coefficients.

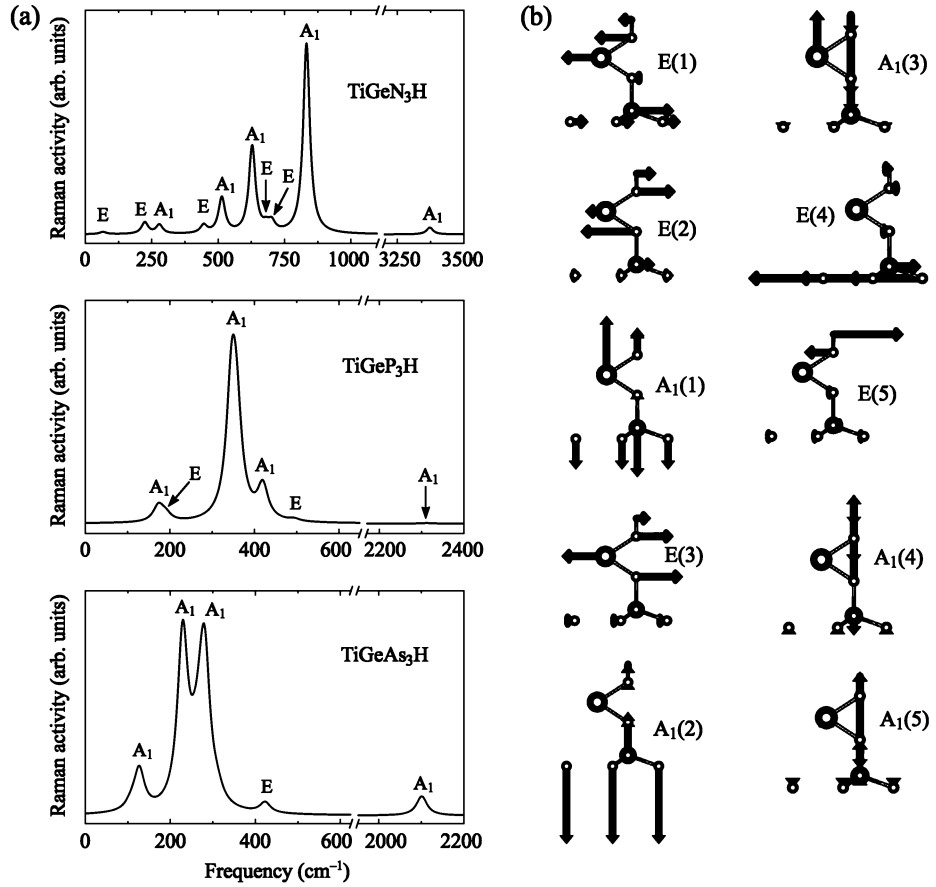

Fig. 3. Calculated Raman spectra of Janus TiGeZ_3H monolayers (a) and displacements of atoms of the optical vibrational modes in Janus $TiGeN_3H$ monolayer (b). The numbers in parentheses indicate the order of the vibrational modes A_1 and E with increasing frequency, namely E(1) < E(2) < ⋯ < E(5) and $A_1(1) < A_1(2) < \cdots < A_1(5)$.

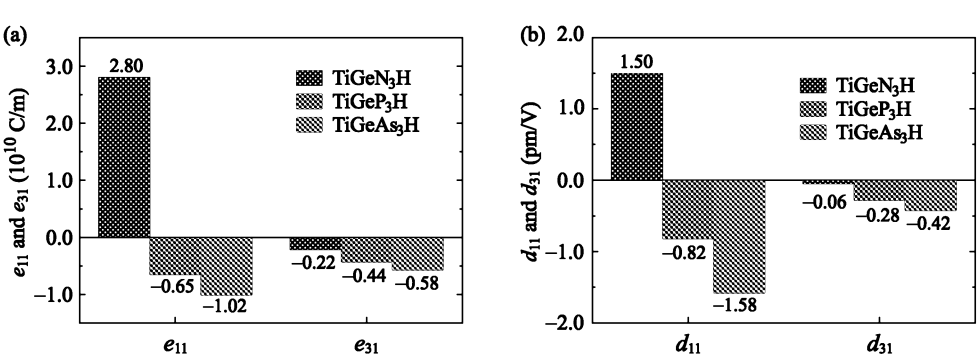

Fig. 4. Calculated piezoelectric coefficients e (a) and d (b) of TiGeZ_3H monolayers.

Janus TiGeZ_3H monolayers exhibit both in-plane (e_{11}) and out-of-plane (e_{31}) piezoelectric responses when subjected to applied strain, due to the breaking of vertical mirror symmetry. The values of piezoelectric strain tensors d_{ij} can be found by using the relations: [51]

$$d_{11} = \frac{e_{11}}{C_{11} - C_{12}}, \tag{7}$$

$$d_{31} = \frac{e_{31}}{C_{11} + C_{12}}. \tag{8}$$

The computed values for piezoelectric coefficients of TiGeZ_3H materials are presented in Table 2. The values of in-plane coefficients $e_{11}(d_{11})$ for $TiGeN_3H$, $TiGeP_3H$, and $TiGeAs_3H$ are computed to be 2.80×10^{10} C/m (1.50 pm/V), -0.65×10^{10} C/m (−0.44 pm/V), and -1.05×10^{10} C/m (−0.58 pm/V), respectively. Obviously, $TiGeN_3H$ monolayer exhibits the highest in-plane piezoelectric coefficients e_{11} and d_{11}. Meanwhile, $TiGeAs_3H$ monolayer possesses the highest value of out-of-plane piezoelectric coefficient d_{31} (absolute value), up to −0.42 pm/V. We show the comparison of piezoelectric coefficients between the structures in Fig. 4. The computed values of d_{31} for TiGeZ_3H, which vary from −0.07 to −0.42 pm/V as listed in Table 2, are comparable to those of similar 2D hexagonal structures, including $MoSiGeN_4$ monolayer (−0.014 pm/V) [16] or Janus structures of group III monochalcogenide monolayers (0.07–0.46 pm/V) [51]. The high piezoelectric responses in TiGeZ_3H monolayers render them a viable contender for implementation in piezoelectric nanodevices.

3.4. Electronic properties

The application prospects of a material are largely determined by its electronic properties. These properties affect how a studied material

Table 3
Bandgaps E_g (eV) calculated by PBE, HSE06, and PBE+SOC method, valley spin splitting λ (meV), Rashba constant α (meV Å), potential difference $\Delta\Phi$ (eV), and work functions Φ_Z (eV) and Φ_H (eV) on the Z and H sides of TiGeZ_3H monolayers.

	E_g^{PBE}	E_g^{HSE06}	$E_g^{PBE+SOC}$	λ_V	λ_C	α_R^K	α_R^M	$\Delta\Phi$	Φ_Z	Φ_H
$TiGeN_3H$	1.84	3.10	1.82	12.50	34.40	–	–	2.65	6.95	4.30
$TiGeP_3H$	0.39	1.20	0.32	26.40	36.30	–	–	2.67	5.24	4.57
$TiGeAs_3H$	0.25	1.07	0.18	130.40	54.50	317.65	360.0	0.21	4.77	4.56

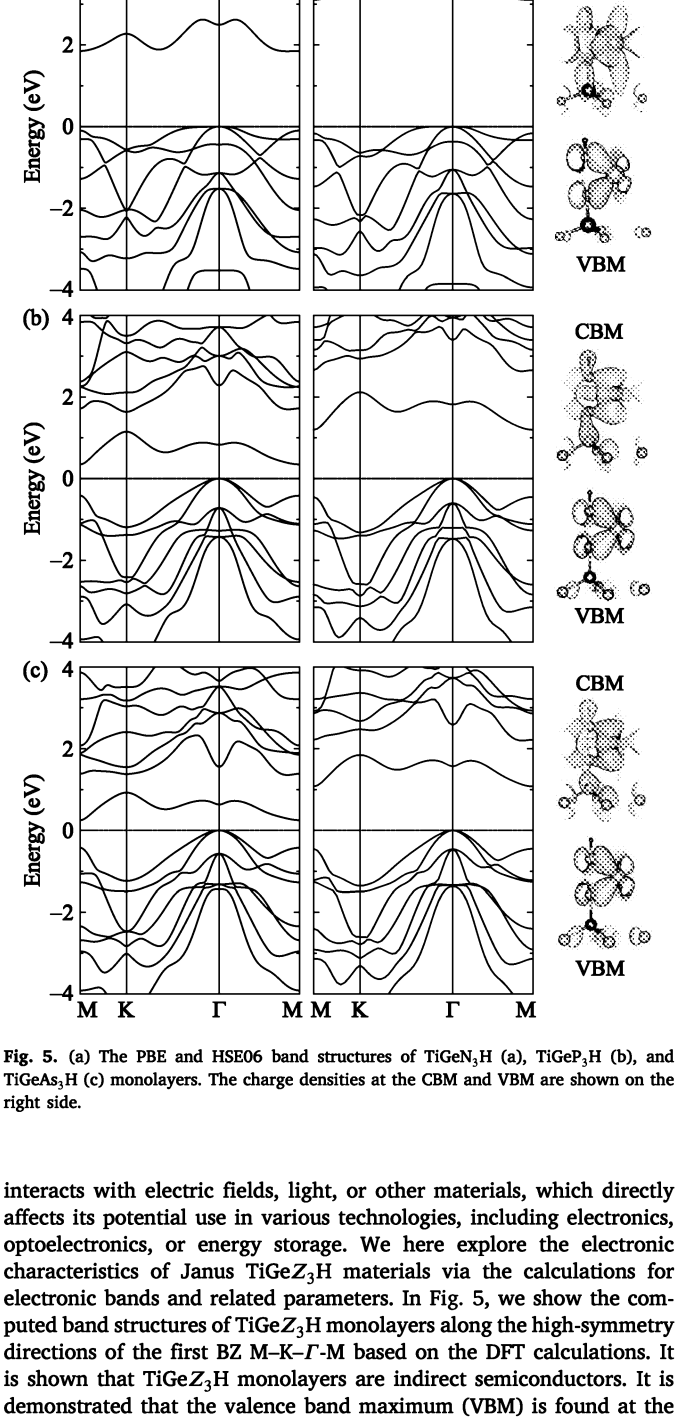

Fig. 5. (a) The PBE and HSE06 band structures of $TiGeN_3H$ (a), $TiGeP_3H$ (b), and $TiGeAs_3H$ (c) monolayers. The charge densities at the CBM and VBM are shown on the right side.

interacts with electric fields, light, or other materials, which directly affects its potential use in various technologies, including electronics, optoelectronics, or energy storage. We here explore the electronic characteristics of Janus TiGeZ_3H materials via the calculations for electronic bands and related parameters. In Fig. 5, we show the computed band structures of TiGeZ_3H monolayers along the high-symmetry directions of the first BZ M–K–Γ-M based on the DFT calculations. It is shown that TiGeZ_3H monolayers are indirect semiconductors. It is demonstrated that the valence band maximum (VBM) is found at the Γ while the conduction band minimum (CBM) is sitting at the M point in the first BZ. At the PBE theoretical level, the bandgaps of $TiGeN_3H$, $TiGeP_3H$, and $TiGeAs_3H$ monolayers are computed to be 1.84, 0.39, and 0.25 eV, respectively. For comparison, the computed bandgap of TiGeZ_3H is wider than that of TiGe2Z_3 (the PBE bandgap of $TiGeN_4$ is 0.82 eV and both $TiGeP_4$ and $TiGeAs_4$ are metallic) [8]. The PBE functional in DFT simulations, however, underestimates the accuracy of the semiconductor bandgap. Therefore, to correct the bandgap of the investigated structures, we also calculate the band structures of TiGeZ_3H monolayers by using the HSE06 functional. It is found that the HSE06 bandgaps of $TiGeN_3H$, $TiGeP_3H$, and $TiGeAs_3H$ monolayers are 3.10, 1.20, and 1.07 eV, respectively. The HSE06 bandgap of TiGeZ_3H is much wider than its PBE bandgap, however, the profiles of the PBE and HSE06 band diagrams are quite similar as illustrated in Fig. 5. Along with the band structures, the charge densities at the CBM and VBM of Janus TiGeZ_3H are also shown in Fig. 5. In the case of Janus $TiGeN_3H$ monolayer, the charge density of the CBM is significantly distributed among Ti atom, and N–H and Ge–N bonds. Meanwhile, the charge density of the VBM is distributed among the upper Ti–N bond. The charge densities of the VBM of $TiGeP_3H$ and $TiGeAs_3H$ are distributed among the lower Ti–N bond while the charge density of the CBM of $TiGeP_3H$ ($TiGeAs_3H$) is distributed among the Ti–N bonds (Ge–N and N–H bonds).

Spin–orbit coupling (SOC) is a crucial factor in determining the electronic characteristics of nanomaterials, especially in materials with heavy elements or large atomic numbers. It not only alters the electronic band structure but also enables new functionalities such as control and manipulation of spin. Understanding and harnessing the SOC effect are crucial for the development of advanced spintronic devices and for exploring emerging quantum phenomena in nanostructures. In momentum space, SOC causes the splitting of electronic bands of materials due to the interaction between the spin of an electron and its motion. In heavy-based compounds, this spin-splitting can result in significant modifications to the electronic band structure. Particularly, in the structural asymmetry, SOC can generate spin-dependent electronic characteristics, including the Rashba and Dresselhaus effects. These phenomena result in spin polarization and can be utilized for spintronics applications, such as spin-based electronic devices or information storage. To evaluate the influence of SOC on the electronic characteristics of TiGeZ_3H monolayers, we calculate their band structures using the PBE+SOC method as shown in Fig. 6. When SOC is included, the spin degeneracy is eliminated and there is spin splitting in the band structures of TiGeZ_3H monolayers. Obviously, the influence of SOC on $TiGeAs_3H$ is stronger than on the other two structures due to the larger atomic size of As. In the presence of the SOC effect, the bandgap of $TiGeAs_4$ decreases sharply, reaching 0.18 eV, which is much narrower than it PBE gap (0.25 eV) as listed in Table 3. Meanwhile, the SOC effect only slightly reduces the bandgaps of $TiGeN_3H$ and $TiGeP_3H$ monolayers. The bandgaps of $TiGeN_4$ and $TiGeP_4$ monolayers are computed to be 1.82 and 0.32 eV, respectively. Furthermore, a small valley spin splitting λ is available at K point in both valence (λ_V) and conduction (λ_C) bands of the studied structures. The computed values of $\lambda_V(\lambda_C)$ for $TiGeN_3H$, $TiGeP_3H$, and $TiGeP_3H$ monolayers are 12.50(34.40), 26.40(36.30), and 130.40(54.50 meV), respectively. It is clear that the influence of SOC on the electronic structure of $TiGeN_3H$ and $TiGeP_3H$ monolayers is insignificant compared to that of $TiGeAs_3H$. In the case of $TiGeAs_3H$, besides having a valley spin splitting λ at the K point, we also observe Rashba-type splitting at the high symmetry point Γ of the conduction band in the reciprocal space as shown in Fig. 6(c). The model for Rashba spin splitting is also illustrated in Fig. 6(c), in which the Rashba effect is quantitatively investigated through three parameters, namely Rashba energy E_R, momentum offset k_R, and Rashba constant α_R. While both E_R and k_R can be obtained

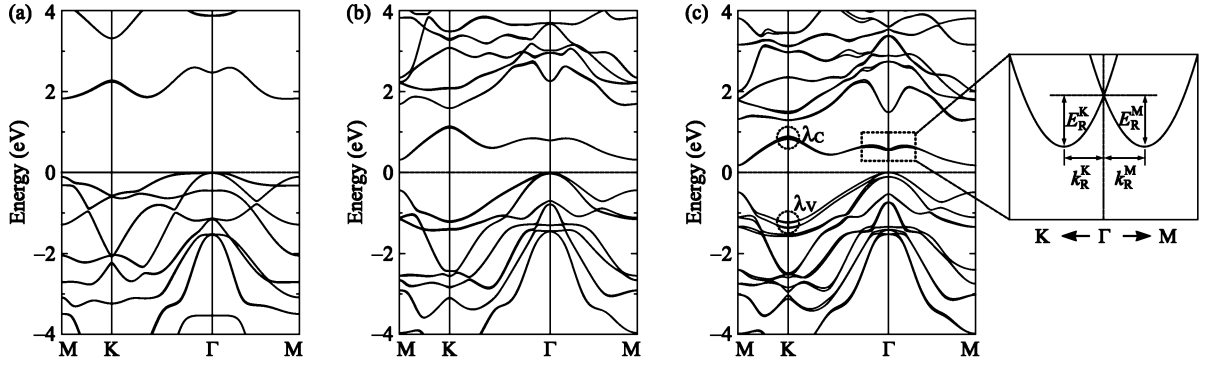

Fig. 6. Band structures of $TiGeN_3H$ (a), $TiGeP_3H$ (b), and $TiGeAs_3H$ (c) monolayers calculated by PBE+SOC method. An illustration of the Rashba SOC splitting is shown in (c).

directly from the electronic band, the value of α_R can be calculated based on the formula as $\alpha_R = 2E_R/k_R$ [52,53]. It is computed that $TiGeAs_3H$ possesses the same Rashba energy of 2.70 meV in the Γ-K and Γ-M directions, namely $E_R^K = E_R^M = 2.70$ meV. Meanwhile, a very slight difference in the momentum offsets k_R^M and k_R^K is found in the Rashba spin splitting of $TiGeAs_3H$. It is calculated to be $k_R^K = 0.017$ Å^{-1} and $k_R^M = 0.015$ Å^{-1}. As revealed in Table 3, Rashba constants α_R^K and α_R^M for $TiGeAs_3H$ are computed to be 317.65 and 360.0 meV Å, respectively. These obtained values for Rashba constants of $TiGeAs_3H$ are comparable to those of Janus MoSSe (479 meV Å) or MoSeTe (322 meV Å) [53]. It is clear that the difference in Rashba parameters in the Γ-K and Γ-M directions of $TiGeAs_3H$ is insignificant. We can roughly conclude that the Rashba parameters exhibit limited sensitivity to the investigated directions in the reciprocal space for $TiGeAs_3H$ monolayer.

Another important characteristic of electronics that we examine in this section is work function. The work function reveals the energy required to remove an electron from the Fermi level to a point outside the material, typically in a vacuum. We can calculate the work function Φ based on the analysis of electrostatic potential with the characteristic parameters being the vacuum energy level E_{vac} and obtained Fermi energy level E_F via the expression as $\Phi = E_{vac} - E_F$. Understanding the relationship between electrostatic potential and work function is essential for tailoring the electronic features of 2D nanostructures and designing novel 2D material-based electronic and optoelectronic nanodevices. In Fig. 7, we present the computed results for the electrostatic potentials via length along the z direction with dipole corrections of Janus $TiGeZ_3H$ monolayers. Due to the vertical asymmetric crystal structure, there is a distinct potential difference $\Delta\Phi$ between the two surfaces of the studied structures as shown in Fig. 7. It is noted that the presence of out-of-plane inversion asymmetry in Janus materials leads to the generation of intrinsic electric fields in the vertical direction (the z direction) [54]. This field has the potential to enhance the separation of electron–hole pairs, which is useful for applications in photocatalytic water-splitting. In the case of Janus structure is under an external electric field applied in the out-of-plane direction, it interacts with the intrinsic field and can influence the electronic structure. The external field can additionally alter the band structure, potentially reducing or expanding the band gap. This effect is contingent upon the alignment of the applied field with respect to the built-in field. The intrinsic dipole moment of the Janus structure may be either amplified or diminished, contingent upon the orientation of the applied field. This influences charge distribution, displacing electron and hole densities to opposing sides of the structure.

The computed potential difference $\Delta\Phi$ for $TiGeN_3H$, $TiGeP_3H$, and $TiGeP_3H$ monolayers are 2.65, 2.67, and 0.21 eV, respectively. As presented in Table 3, the work function on the H side is lower than that on the other side for all three examined materials, demonstrating the easier escape of electrons on the H side compared to the other side.

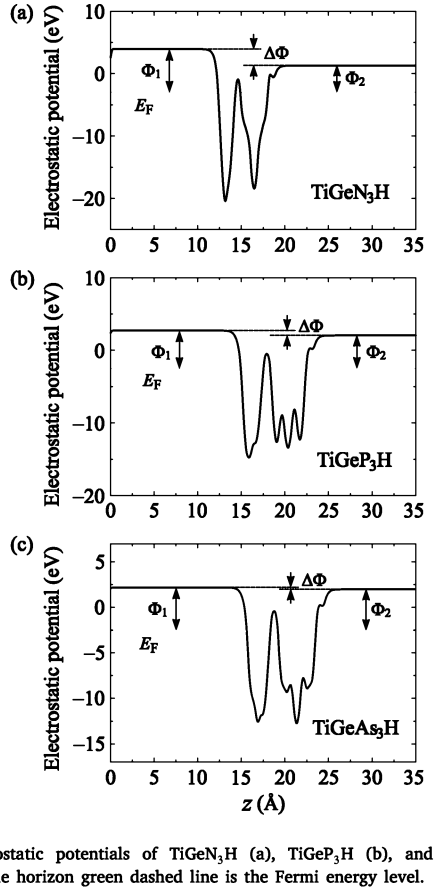

Fig. 7. Electrostatic potentials of $TiGeN_3H$ (a), $TiGeP_3H$ (b), and $TiGeAs_3H$ (c) monolayers. The horizon green dashed line is the Fermi energy level.

3.5. Transport properties

Transport properties are fundamental to the application potential of materials across various fields of technology. A thorough understanding of transport characteristics, especially carrier mobility, allows us to design materials that meet specific functional and technological requirements. We examine the transport features of the Janus $TiGeZ_3H$ materials in this last part. The transport features, especially carrier mobility, play an important role in determining the application prospects of the proposed structures in electronic devices. We here calculate the carrier mobility and other transport features of $TiGeZ_3H$ materials. The carrier mobilities can be accomplished by employing the deformation potential (DP) approximation proposed by Bardeen

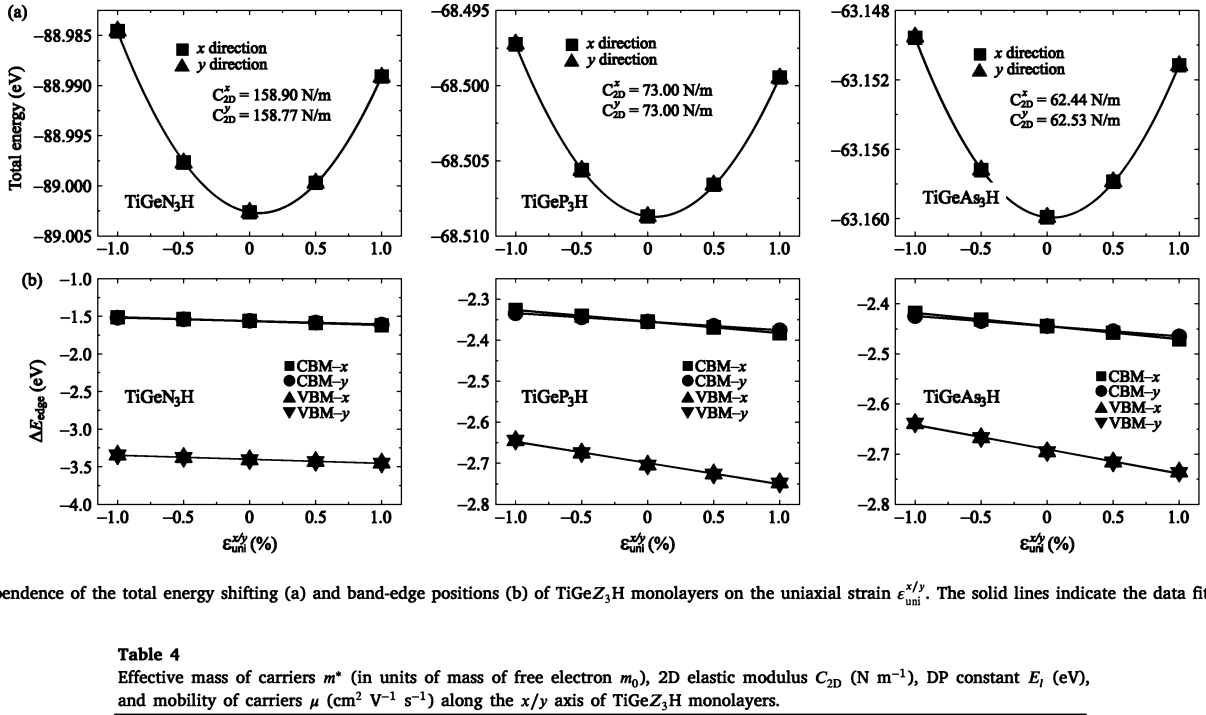

Fig. 8. Dependence of the total energy shifting (a) and band-edge positions (b) of TiGeZ_3H monolayers on the uniaxial strain $\epsilon^{x/y}_{uni}$. The solid lines indicate the data fitting curves.

Table 4
Effective mass of carriers m^* (in units of mass of free electron m_0), 2D elastic modulus C_{2D} (N m^{-1}), DP constant E_l (eV), and mobility of carriers μ (cm^2 V^{-1} s^{-1}) along the x/y axis of TiGeZ_3H monolayers.

		m^*_x	m^*_y	C^x_{2D}	C^y_{2D}	E^x_l	E^y_l	μ_x	μ_y
Electron	TiGeN$_3$H	3.21	5.68	158.90	158.77	−5.28	−4.52	8.84	6.81
	TiGeP$_3$H	0.51	1.49	73.00	73.00	−2.08	−2.48	434.75	275.72
	TiGeAs$_3$H	0.52	1.49	62.44	62.53	−2.63	−2.03	418.88	246.73
Hole	TiGeN$_3$H	5.68	61.70	158.90	158.77	−5.34	−5.42	1.12	0.10
	TiGeP$_3$H	1.11	1.64	73.00	73.00	−5.14	−5.23	39.30	25.62
	TiGeAs$_3$H	1.07	1.49	62.44	62.53	−4.83	−4.91	41.92	29.20

and Shockley [33]. The carrier mobilities in 2D structures μ_{2D} can be written as follows [55]:

$$\mu_{2D} = \frac{e\hbar^3 C_{2D}}{k_B T m^* \overline{m^*} E_l^2}, \tag{9}$$

where the elastic modulus is denoted by C_{2D}; E_l refers to the DP constant; and temperature $T = 300$ K is set in the present calculation. e, $\hbar$, and k_B stand for the elementary charge, reduced Planck's constant, and Boltzmann's constant, respectively; the effective carrier mass is denoted by m^* and $\overline{m^*} = \sqrt{m^*_x m^*_y}$.

To obtain the values of the carrier mobility, we need to calculate the transport parameters m^*, C_{2D}, and E_d through the following expressions:

$$\frac{1}{m^*} = \frac{1}{\hbar^2}\left|\frac{\partial^2 E(k)}{\partial k^2}\right|, \tag{10}$$

$$C_{2D} = \frac{1}{\Omega}\frac{\partial^2 E_{tot}}{\partial \epsilon^2_{uni}}, \tag{11}$$

$$E_l = \frac{\Delta E_{edge}}{\epsilon_{uni}}, \tag{12}$$

where symbol $E(k)$ represents the energy at the VBM/CBM that depends on the wavevector k, Ω indicates the area of the optimized unitcell, E_{tot} is the total energy, ϵ_{uni} stands for the applied uniaxial strain along the x/y-axis, and ΔE_{edge} is the change in the position of the VBM/CBM relative to the vacuum energy level.

The computed values for m^* along the two transport directions x and y are revealed in Table 4. It is found that TiGeN$_3$H exhibits high effective masses, both electron and hole. This is an important point that allows us to predict that the carriers in TiGeN$_3$H may have low mobility because once the mass of the carrier is large, its ability to react to the external field will slow down. Of course, the carrier mobility depends not only on m but also on other parameters as released in Eq. (10). The high values of m^* in TiGeN$_3$H are consistent with the obtained band diagram of TiGeN$_3$H as revealed in Fig. 5, that the larger the radius of curvature of the band diagram around the band edges (the CBM for electrons and VBM for the holes), the larger the carrier mass. This is because the mass is inversely proportional to the $\partial^2 E(k)/\partial k^2$ as shown in Eq. (10). As revealed in Table 4, we can see that TiGeN$_3$H has directionally anisotropic effective masses. The computed m^* along the x and y axes for TiGeN$_3$H is found to be $3.21m_0$ and $5.68m_0$ (m_0 refers to the free electron mass), respectively. Meanwhile, both TiGeP$_3$H and TiGeAs$_3$H have a lower electron mass. Consequently, TiGeN$_3$H can be very low carrier mobility. In Table 4, we also show the computed results for the C_{2D} and E_d, which can be obtained via the fitting the uniaxial strain-dependence of the energy shifts and band edge positions as depicted in Fig. 8. The electron mobility along the x axis μ_x for TiGeN$_3$H is found to be only 8.84 cm^2 V^{-1} s^{-1} while the computed values of μ_x for TiGeP$_3$H and TiGeAs$_3$H monolayers are up to 434.75 and 418.88 cm^2 V^{-1} s^{-1}, respectively. With high electron mobility, TiGeP$_3$H and TiGeAs$_3$H monolayers are suitable for applications in nanoelectronics.

4. Conclusion

In conclusion, we proposed and thoroughly examined the physical properties of Janus TiGeZ_3H monolayers using the first-principles method. By analyzing the phonon spectra and AIMD tests, all three proposed Janus TiGeZ_3H monolayers are confirmed to be structurally stable. Further, the mechanical stability of TiGeZ_3H monolayers was confirmed with the Born–Huang mechanical stability criterion. Our examinations for the vibrational characteristics revealed that there are ten Raman active modes, including five A_1 and five E optical modes, in Janus TiGeZ_3H structure. In each Janus structure, the most prominent Raman peaks are A_1 mode and the redshift is observed in the Raman

spectra of TiGeZ_3H when the atomic size of the Z atom increases from N to As. Janus TiGeZ_3H monolayers exhibited as good piezoelectric materials with the presence of both in-plane and out-of-plane piezoelectric responses due to their vertical asymmetric structure. While $TiGeN_3H$ monolayer exhibits a high in-plane piezoelectric (d_{11} = 1.50 pm/V), possesses an impressive out-of-plane piezoelectric coefficient d_{31} value of $TiGeAs_3H$ up to −0.42 pm/V. At the ground state, Janus TiGeZ_3H monolayers are semiconductors with the indirect bandgap varying from 1.07 to 3.10 eV based on the calculations at the HSE06 theoretical level. Moreover, Rashba spin splitting was found in Janus $TiGeAs_3H$ when the SOC was taken into account. Particularly, Janus $TiGeP_3H$ and $TiGeAs_3H$ monolayers possess electrons with high mobility, exceeding 400 $cm^2 V^{-1} s^{-1}$, which is advantageous for their application in nanoelectronics. Our findings not only provide the basic physical characteristics of Janus TiGeZ_3H but also provide an important theoretical basis as a premise for further study as well as the prospect for their application in various fields of nanoscale devices.

CRediT authorship contribution statement

A.I. Kartamyshev: Visualization, Software, Methodology, Investigation, Formal analysis, Data curation. **Nguyen N. Hieu:** Writing – review & editing, Writing – original draft, Validation, Supervision, Resources, Investigation, Formal analysis, Conceptualization. **N.A. Poklonski:** Writing – original draft, Validation, Investigation, Funding acquisition, Formal analysis, Conceptualization. **Nguyen V. Hieu:** Validation, Methodology, Investigation, Formal analysis, Conceptualization. **Tuan V. Vu:** Visualization, Validation, Methodology, Investigation, Formal analysis, Conceptualization. **A.A. Lavrentyev:** Validation, Methodology, Investigation, Formal analysis, Conceptualization. **Huynh V. Phuc:** Writing – review & editing, Writing – original draft, Visualization, Validation, Investigation, Formal analysis, Conceptualization.

Declaration of competing interest

I declare that I have no significant competing financial, professional, or personal interests that might have influenced the performance or presentation of the work described in this manuscript.

Acknowledgments

N.A.P. was supported by the Belarusian Republican Foundation for Fundamental Research, Republic of Belarus (Grant number F23RNF-049) and Belarusian National Research Program "Convergence-2025".

Data availability

Data will be made available on request.

References

[1] K.S. Novoselov, A.K. Geim, S.V. Morozov, D. Jiang, Y. Zhang, S.V. Dubonos, I.V. Grigorieva, A.A. Firsov, Electric field effect in atomically thin carbon films, Science 306 (2004) 666.

[2] N.A. Poklonski, S.A. Vyrko, A.I. Siahlo, O.N. Poklonskaya, S.V. Ratkevich, N.N. Hieu, A.A. Kocherzhenko, Synergy of physical properties of low-dimensional carbon-based systems for nanoscale device design, Mater. Res. Express 6 (4) (2019) 042002.

[3] T.C. Phong, L.T.T. Phuong, Tuning electronic phase of monolayer β_{12}-borophene via adsorbed gas molecules: Generation of van hove singularity, Physica B 666 (2023) 415119.

[4] T.C. Phong, N.T. Nam, L.T.T. Phuong, Tuning the van Hove singularities in monolayer PbBiI via C_{3v} symmetry breaking, Phys. Lett. A 474 (2023) 128830.

[5] K.S. Novoselov, D. Jiang, F. Schedin, T.J. Booth, V.V. Khotkevich, S.V. Morozov, A.K. Geim, Two-dimensional atomic crystals, Proc. Natl. Acad. Sci. USA 102 (2005) 10451–10453.

[6] F. Schwierz, J. Pezoldt, R. Granzner, Two-dimensional materials and their prospects in transistor electronics, Nanoscale 7 (18) (2015) 8261–8283.

[7] Y.-L. Hong, Z. Liu, L. Wang, T. Zhou, W. Ma, C. Xu, S. Feng, L. Chen, M.-L. Chen, D.-M. Sun, X.-Q. Chen, H.-M. Cheng, W. Ren, Chemical vapor deposition of layered two-dimensional MoS_2N_4 materials, Science 369 (6504) (2020) 670–674.

[8] L. Wang, Y. Shi, M. Liu, A. Zhang, Y.-L. Hong, R. Li, Q. Gao, M. Chen, W. Ren, H.-M. Cheng, Y. Li, X.-Q. Chen, Intercalated architecture of ma2z4 family layered van der waals materials with emerging topological, magnetic and superconducting properties, Nature Commun. 12 (1) (2021) 2361.

[9] Y. Wang, S.-S. Wang, Y. Lu, J. Jiang, S.A. Yang, Strain-induced isostructural and magnetic phase transitions in monolayer MoN_2, Nano Lett. 16 (7) (2016) 4576–4582.

[10] Z. Deng, Electric field enhancement effect on Raman spectra in two-dimensional $MoSi_2N_4$, $TiSi_2N_4$ and $MoGe_2As_4$ monolayers, Solid State Commun. 358 (2022) 114994.

[11] J. Yu, J. Zhou, X. Wan, Q. Li, High intrinsic lattice thermal conductivity in monolayer $MoSi_2N_4$, New J. Phys. 23 (3) (2021) 033005.

[12] L. Cao, G. Zhou, Q. Wang, L.K. Ang, Y.S. Ang, Two-dimensional van der waals electrical contact to monolayer $MoSi_2N_4$, Appl. Phys. Lett. 118 (2021) 013106.

[13] X. Xu, L. Yang, Q. Gao, X. Jiang, D. Li, B. Cui, D. Liu, Type-ii mosi2n4/mos2 van der waals heterostructure with excellent optoelectronic performance and tunable electronic properties, J. Phys. Chem. C 127 (16) (2023) 7878–7886.

[14] C. Nguyen, N.V. Hoang, H.V. Phuc, A.Y. Sin, C.V. Nguyen, Two-dimensional boron phosphide/moge2n4 van der waals heterostructure: A promising tunable optoelectronic material, J. Phys. Chem. Lett. 12 (21) (2021) 5076–5084.

[15] R. Sibatov, R. Meftakhutdinov, A. Kochaev, Asymmetric $XMoSiN_2$ (X=S, Se, Te) monolayers as novel promising 2d materials for nanoelectronics and photovoltaics, Appl. Surf. Sci. 585 (2022) 152465.

[16] S.-D. Guo, W.-Q. Mu, Y.-T. Zhu, R.-Y. Han, W.-C. Ren, Predicted septuple-atomic-layer janus MSiGeN4 (m=mo and w) monolayers with rashba spin splitting and high electron carrier mobilities, J. Mater. Chem. C 9 (7) (2021) 2464–2473.

[17] X. Guo, S. Guo, Janus $MSiGeN_4$ (M=Zr and Hf) monolayers derived from centrosymmetric β-MA_2Z_4: A first-principles study, J. Semicond. 42 (12) (2021) 122002.

[18] J. Zhang, S. Jia, I. Kholmanov, L. Dong, D. Er, W. Chen, H. Guo, Z. Jin, V.B. Shenoy, L. Shi, J. Lou, Janus monolayer transition-metal dichalcogenides, ACS Nano 11 (8) (2017) 8192–8198.

[19] A.-Y. Lu, H. Zhu, J. Xiao, C.-P. Chuu, Y. Han, M.-H. Chiu, C.-C. Cheng, C.-W. Yang, K.-H. Wei, Y. Yang, Y. Wang, D. Sokaras, D. Nordlund, P. Yang, D.A. Muller, M.-Y. Chou, X. Zhang, L.-J. Li, Janus monolayers of transition metal dichalcogenides, Nat. Nanotechnol. 12 (2017) 744.

[20] V.T.T. Vi, T.P.T. Linh, C.Q. Nguyen, N.N. Hieu, Tunable electronic properties of novel 2D Janus $MSiGeN_4$ (M = Ti, Zr, Hf) monolayers by strain and external electric field, Adv. Theory Simul. 5 (11) (2022) 2200499.

[21] S.-T. Nguyen, C.Q. Nguyen, Y.S. Ang, H.V. Phuc, N.N. Hieu, N.T. Hiep, N.M. Hung, L.T.T. Phuong, N.V. Hieu, C.V. Nguyen, Tunable schottky contact at the graphene/Janus $SMoSiN_2$ interface for high-efficiency electronic devices, J. Phys. D: Appl. Phys. 56 (4) (2022) 045306.

[22] C.C. Tho, S.-D. Guo, S.-J. Liang, W.L. Ong, C.S. Lau, L. Cao, G. Wang, Y.S. Ang, MA_2Z_4 family heterostructures: Promises and prospects, Appl. Phys. Rev. 10 (4) (2023) 041307.

[23] M. Yagmurcukardes, Y. Qin, S. Ozen, M. Sayyad, F.M. Peeters, S. Tongay, H. Sahin, Quantum properties and applications of 2D janus crystals and their superlattices, Appl. Phys. Rev. 7 (1) (2020) 011311.

[24] P.E. Blöchl, Projector augmented-wave method, Phys. Rev. B 50 (1994) 17953.

[25] G. Kresse, D. Joubert, From ultrasoft pseudopotentials to the projector augmented-wave method, Phys. Rev. B 59 (3) (1999) 1758–1775.

[26] G. Kresse, J. Furthmüller, Efficient iterative schemes for *ab initio* total-energy calculations using a plane-wave basis set, Phys. Rev. B 54 (16) (1996) 11169–11186.

[27] G. Kresse, J. Furthmüller, Efficiency of ab-initio total energy calculations for metals and semiconductors using a plane-wave basis set, Comput. Mater. Sci. 6 (1) (1996) 15–50.

[28] J.P. Perdew, K. Burke, M. Ernzerhof, Generalized gradient approximation made simple, Phys. Rev. Lett. 77 (18) (1996) 3865.

[29] J. Heyd, G.E. Scuseria, M. Ernzerhof, Hybrid functionals based on a screened coulomb potential, J. Chem. Phys. 118 (18) (2003) 8207.

[30] A.H. MacDonald, W.E. Picket, D.D. Koelling, A linearised relativistic augmented-plane-wave method utilising approximate pure spin basis functions, J. Phys. C: Solid State Phys. 13 (14) (1980) 2675.

[31] A. Togo, L. Chaput, I. Tanaka, Distributions of phonon lifetimes in brillouin zones, Phys. Rev. B 91 (9) (2015) 094306.

[32] M. Yagmurcukardes, F.M. Peeters, H. Sahin, Electronic and vibrational properties of PbI_2: From bulk to monolayer, Phys. Rev. B 98 (8) (2018) 085431.

[33] J. Bardeen, W. Shockley, Deformation potentials and mobilities in non-polar crystals, Phys. Rev. 80 (1) (1950) 72.

[34] T.V. Vu, V.T.T. Vi, N.T. Hiep, K.V. Hoang, A.I. Kartamyshev, H.V. Phuc, N.N. Hieu, A first-principles prediction of novel Janus $ZrGeZ_3H$ (Z = N, P, and As) monolayers: Raman active modes, piezoelectric responses, electronic properties, and carrier mobility, RSC Adv. 14 (2024) 21982.

[35] H. Li, Q. Zhang, C.C.R. Yap, B.K. Tay, T.H.T. Edwin, A. Olivier, D. Baillargeat, From bulk to monolayer mos2: Evolution of raman scattering, Adv. Funct. Mater. 22 (7) (2012) 1385–1390.

[36] M. Materano, P. Reinig, A. Kersch, M. Popov, M. Deluca, T. Mikolajick, U. Boettger, U. Schroeder, Raman spectroscopy as a key method to distinguish the ferroelectric orthorhombic phase in thin ZrO_2-based films, Phys. Status Solidi - Rapid Res. Lett. 16 (4) (2022) 2100589.

[37] P. Goj, A. Wajda, P. Stoch, Raman imaging as a useful tool to describe crystallization of aluminum/iron-containing polyphosphate glasses, J. Eur. Ceram. Soc. 41 (8) (2021) 4572–4583.

[38] X. Zhang, Characterization of layer number of two-dimensional transition metal diselenide semiconducting devices using si-peak analysis, Adv. Mater. Sci. Eng. 2019 (2019) 1–7.

[39] X. Li, Y. Shi, S. Li, W. Shi, W. Han, C. Zhou, X. Zhao, B. Liang, Layer-number dependent reflection spectra of MoS_2 flakes on SiO_2/Si substrate, Opt. Mater. Express 8 (10) (2018) 3082.

[40] N.S. Taghavi, P. Gant, P. Huang, I. Niehues, R. Schmidt, S. Michaelis de Vasconcellos, R. Bratschitsch, M. García-Hernández, R. Frisenda, A. Castellanos-Gomez, Thickness determination of MoS_2, $MoSe_2$, WS_2 and WSe_2 on transparent stamps used for deterministic transfer of 2D materials, Nano Res. 12 (7) (2019) 1691–1695.

[41] M. Jahangirzadeh Varjovi, S. Ershadrad, B. Sanyal, S. Tosoni, Two-dimensional MSi_2N_4 (M = Ge, Sn, and Pb) monolayers: promising new materials for optoelectronic applications, 2D Mater. 11 (1) (2023) 015016.

[42] K.-A.N. Duerloo, M.T. Ong, E.J. Reed, Intrinsic piezoelectricity in two-dimensional materials, J. Phys. Chem. Lett. 3 (19) (2012) 2871–2876.

[43] M. Born, K. Huang, Dynamical theory of crystal lattices, Am. J. Phys. 23 (7) (1955) 474.

[44] R.C. Andrew, R.E. Mapasha, A.M. Ukpong, N. Chetty, Mechanical properties of graphene and boronitrene, Phys. Rev. B 85 (12) (2012) 125428.

[45] T. Wu, H. Zhang, Piezoelectricity in two-dimensional materials, Angew. Chem. Int. Ed. Engl. 54 (15) (2015) 4432–4434.

[46] T.V. Vu, H.V. Phuc, A.I. Kartamyshev, N.N. Hieu, Enhanced out-of-plane piezoelectricity and carrier mobility in janus γ-Sn_2XY (X/Y = S, Se, Te) monolayers: A first-principles prediction, Appl. Phys. Lett. 122 (6) (2023) 061601.

[47] F. Li, T. Shen, C. Wang, Y. Zhang, J. Qi, H. Zhang, Recent advances in strain-induced piezoelectric and piezoresistive effect-engineered 2d semiconductors for adaptive electronics and optoelectronics, Nano-Micro Lett. 12 (2020) 106.

[48] M.N. Blonsky, H.L. Zhuang, A.K. Singh, R.G. Hennig, Ab initio prediction of piezoelectricity in two-dimensional materials, ACS Nano 9 (10) (2015) 9885–9891.

[49] H. Zhu, Y. Wang, J. Xiao, M. Liu, S. Xiong, Z.J. Wong, Z. Ye, Y. Ye, X. Yin, X. Zhang, Observation of piezoelectricity in free-standing monolayer MoS_2, Nat. Nanotechnol. 10 (2) (2014) 151–155.

[50] R.D. King-Smith, D. Vanderbilt, Theory of polarization of crystalline solids, Phys. Rev. B 47 (3) (1993) 1651–1654.

[51] Y. Guo, S. Zhou, Y. Bai, J. Zhao, Enhanced piezoelectric effect in janus group-iii chalcogenide monolayers, Appl. Phys. Lett. 110 (16) (2017) 163102.

[52] S. Singh, A.H. Romero, Giant tunable rashba spin splitting in a two-dimensional bisb monolayer and in BiSb/AlN heterostructures, Phys. Rev. B 95 (16) (2017) 165444.

[53] T. Hu, F. Jia, G. Zhao, J. Wu, A. Stroppa, W. Ren, Intrinsic and anisotropic Rashba spin splitting in janus transition-metal dichalcogenide monolayers, Phys. Rev. B 97 (23) (2018) 235404.

[54] C.-F. Fu, J. Sun, Q. Luo, X. Li, W. Hu, J. Yang, Intrinsic electric fields in two-dimensional materials boost the solar-to-hydrogen efficiency for photocatalytic water splitting, Nano Lett. 18 (10) (2018) 6312–6317.

[55] W. Wan, S. Zhao, Y. Ge, Y. Liu, Phonon and electron transport in janus monolayers based on inse, J. Phys.: Condens. Matter 31 (43) (2019) 435501.